



Selective oxidation of methane to CO on Ni@BO_x via reaction-induced vapor migration of boron-containing species onto Ni

Tongyuan Song^{a,b}, Rongtan Li^{a,b}, Jianyang Wang^{a,c}, Cui Dong^{a,c}, Xiaohui Feng^{a,d},
Shiwen Li^{a,b}, Rentao Mu^{a,c}, Qiang Fu^{a,c,*}

^a State Key Laboratory of Catalysis, iChEM, Dalian Institute of Chemical Physics, the Chinese Academy of Science, Dalian 116023, China

^b University of Chinese Academy of Sciences, Beijing 100049, China

^c Dalian National Laboratory for Clean Energy, Dalian Institute of Chemical Physics, the Chinese Academy of Sciences, Dalian 116023, China

^d University of Science and Technology of China, Hefei 230026, China

ARTICLE INFO

Keywords:

Selective oxidation of methane
Strong metal-support interaction
Hexagonal boron nitride
Vapor migration

ABSTRACT

Dynamic migration of support-derived species and subsequent encapsulation of supported metal nanoparticles (NPs) are the well-known features of the Strong Metal-Support Interaction (SMSI) effect. Here, we report occurrence of the classical SMSI state in physical mixture of Ni NPs and porous hexagonal boron nitride powder (Ni/pBN) during methane oxidation reaction at 600 °C, in which Ni NPs are encapsulated by BO_x overlayers derived from the pBN component. The SMSI state can switch the methane oxidation selectivity from CO₂ on the fresh Ni/pBN catalyst to CO on the used catalyst. The encapsulation of Ni NPs by BO_x overlayers has also been observed in Ni/Al₂O₃ catalyst which is physically mixed with pBN. Comprehensive characterizations confirm that the SMSI state is induced by vapor migration of boron-containing species e.g. BO_xH_y from pBN to metal surfaces, in which both high reaction temperature and water product play an important role.

1. Introduction

Methane is the main component of natural gas and a major greenhouse gas [1,2]. The catalytic combustion of methane to carbon dioxide and partial oxidation of methane to syngas are the effective ways to reduce the greenhouse effect caused by methane [3–5]. Ni presents comparable activity to noble metals for catalytic oxidation of methane, while thermal stability and coking resistance of Ni-based catalysts still hinder their applications. The previous works have demonstrated that the Ni-catalyzed performance in the catalytic oxidation of methane can be significantly improved by utilizing the interaction of Ni catalysts with suitable supports such as CeO₂, ZnO, and hexagonal boron nitride (h-BN) [6–11]. However, the evolution of the interfacial structure of both metal and support during the reaction needs to be further explored, which is also an important research direction for the Strong Metal-Support Interaction (SMSI) effect [12–16].

The migration of support-derived species onto the surface of metal nanoparticles (NPs) to form an ultrathin overlayer is the typical characteristic of the SMSI effect, which has been widely observed on group VIII metals supported on transition metal oxides (TiO₂, Fe₃O₄, CeO₂,

etc.) upon high-temperature reduction treatments [17–26]. Generally, the encapsulation structure can block the metal active sites, which can inhibit the catalytic activity of metals [27,28]. However, in some cases the resulting encapsulated overlayers can be used to modify the catalytic performance in various metal-catalyzed reactions, which has been utilized to improve catalyst stability and alter product selectivity [11, 28–33]. Tang et al. found that the stability of Au/TiO₂ catalysts in CO oxidation and hydrocarbon combustion reactions has been greatly improved by constructing the classical SMSI state at high temperature reducing atmospheres [28]. Xin et al. constructed a Ru@MoO_{3-x} encapsulation structure during CO₂ hydrogenation reaction, which switches the selectivity of CO₂ hydrogenation from 100 % CH₄ on fresh Ru particles to above 99.0 % CO at the SMSI state [33].

The classical SMSI effect has been recently extended to some unconventional catalyst systems such as Au/ZnO, Ni/h-BN and Au/MgO [11,16,30,33–39]. In these cases, the encapsulation structure has been produced under oxidation or other specific reaction conditions. For example, Liu et al. reported that Au NPs supported on ZnO nanorods could be encapsulated by zinc oxide (ZnO_x) overlayers under oxidation conditions at mild temperatures, in which the formation of Au-O-Zn

* Corresponding author at: State Key Laboratory of Catalysis, iChEM, Dalian Institute of Chemical Physics, the Chinese Academy of Science, Dalian 116023, China.
E-mail address: qfu@dicp.ac.cn (Q. Fu).

bonds plays a key role in ZnO_x migration onto the surface of Au NPs [34]. Dong et al. observed Ni-aided oxidative etching of h-BN nanosheets in dry reforming of methane (DRM) reaction and then migration of boron oxide (BO_x) species onto the Ni NPs forming ultrathin BO_x encapsulation overlayers [11]. Upon the formation of the SMSI state in these systems, the metal NPs are in close contact with the supports and thus support-derived species are supposed to migrate along the metal nanoparticle surface to form the ultrathin encapsulation overlayers [21, 23]. Recently, it has been reported that the SMSI effect can also occur over metal catalysts which are physically mixed with oxides. For example, ZnO_x species were found to migrate from ZnO particles onto Cu particles upon reduction treatment of physical mixture of ZnO and Cu powders in H_2 [40]. Zhang et al. have observed migration of TiO_x onto the surface of large Ni particles, which are physically mixed with anatase TiO_2 particles, and formation of an amorphous TiO_x overlayer on the large Ni particles after treatment in H_2 and at 300 °C [41]. Therefore, the transport of active species from oxide support via direct vapor migration and subsequent deposition onto the metal surface may be active for the SMSI state, which yet needs to be corroborated by solid researches.

In this work, physical mixtures of Ni NPs and porous h-BN support (Ni|pBN) were used in methane oxidation reaction. The classical SMSI state is formed in the Ni|pBN catalyst during the methane oxidation where the selectivity can be reversed from CO_2 to CO at 600 °C due to encapsulation of Ni NPs by BO_x overlayers derived from the pBN support (Ni@ BO_x |pBN). Adding pBN as a diluent to Al_2O_3 supported Ni catalyst (Ni/ Al_2O_3 |pBN) further reduces the contact area between Ni NPs and pBN, while the SMSI effect can still occur under the same reaction condition. Based on ex-situ and in-situ characterizations, it has been revealed that both high reaction temperature and generated water product are indispensable for the formation and vapor migration of BO_x or B(OH)_x species from pBN onto Ni NPs. The reaction induced vapor migration of support-derived species onto the metal surface observed in this work suggests a new path for the SMSI state.

2. Experimental section

2.1. Catalyst preparation

2.1.1. Synthesis of porous h-BN (pBN)

Melamine ($\text{C}_3\text{N}_6\text{H}_6$, Sinopharm Chemical reagent Co., Ltd) and boric acid (H_3BO_3 , Sinopharm Chemical reagent Co., Ltd) were used as a nitrogen source and a boron source, respectively. In a typical process [42, 43], 5.0 g boric acid powder was dissolved in 200 mL deionized water at 60 °C, and then 20.4 g melamine powder was added into the solution and further stirred and heated at 90 °C until all the water was evaporated. The obtained white solid was ground into powder and annealed at 1000 °C under pure NH_3 for 4 h. The obtained white solid was denoted as pBN.

2.1.2. Synthesis of Ni|pBN

The Ni|pBN catalyst was prepared through a physical mixing method. 48 mg commercial nickel oxide powder (Aladdin) and 300 mg pBN powder were ground in an agate mortar for 10 min, and then pretreated in pure H_2 for 1 h at 500 °C (denoted as Ni|pBN).

2.1.3. Synthesis of Ni/ Al_2O_3

The Ni/ Al_2O_3 catalyst was prepared through a physical mixing method. 48 mg commercial nickel oxide powder (Aladdin) and 300 mg commercial Al_2O_3 powder (Alfa) were ground in an agate mortar for 10 min, and then pretreated in pure H_2 for 1 h at 500 °C (denoted as Ni/ Al_2O_3).

2.1.4. Synthesis of Ni/ Al_2O_3

The Ni/ Al_2O_3 catalyst was prepared by an impregnation method. Typically, 0.94 g nickel nitrate hexahydrate ($\text{Ni}(\text{NO}_3)_2 \cdot 6\text{H}_2\text{O}$, Sinopharm Chemical reagent Co., Ltd) was added to 20 mL ethanol. 1.0 g commercial Al_2O_3 powder was impregnated with the $\text{Ni}(\text{NO}_3)_2$ ethanol solution. The suspension was sonicated for 30 min, and further stirred and heated at 40 °C until all ethanol was evaporated. The residual solid was dried overnight at 110 °C. The resulting solid powder was further treated in pure H_2 at 500 °C for 2 h, and the obtained sample was named as Ni/ Al_2O_3 .

2.1.5. Synthesis of Ni/ Al_2O_3 |pBN

Ni/ Al_2O_3 |pBN catalyst was prepared by a physical mixing method. 30 mg pBN powder was added as a diluent to the 60 mg Ni/ Al_2O_3 powder, and then they were mixed by shaking in a reaction tube for 1 min (denoted as Ni/ Al_2O_3 |pBN).

2.1.6. Synthesis of Al_2O_3 |pBN

Al_2O_3 |pBN catalyst was prepared by a physical mixing method. 30 mg pBN powder was added as a diluent to the 60 mg Al_2O_3 powder, and then they were mixed by shaking in a reaction tube for 1 min (denoted as Al_2O_3 |pBN).

2.2. Catalyst characterizations

X-ray diffraction (XRD) patterns were collected on an Empyrean diffractometer using a $\text{Cu K}\alpha$ ($\lambda = 1.5406 \text{ \AA}$) radiation source and scanning rate of 15 °/min. Transmission electron microscopy (TEM) images were recorded on Hitachi HT 7700 microscope operated at an acceleration voltage of 100 kV. High resolution transmission electron microscopy (HRTEM) images were obtained on a JEM-F200 and TECNAI G2 F30 microscope operated at an accelerating voltage of 200 and 300 kV, respectively. Scanning electron microscopy (SEM) images were acquired by JSM-7900F microscope operated at an acceleration voltage of 5 kV. Energy dispersive spectroscopy (EDS) elemental mapping images were obtained using the JEM-F200 and JSM-7900F microscopes. Diffuse reflectance infrared Fourier transform spectroscopic (DRIFTS) spectra were acquired on a Bruker vertex 80 v spectrometer equipped with a Mercury-Cadmium-Tellurium (MCT) detector and a HARRICK heat chamber DiffusIR™ accessory. The DRIFT spectra were obtained in the range of 4000–400 cm^{-1} with a resolution of 4 cm^{-1} and 32 scans. Before collecting CO adsorption signals, each sample was pretreated in pure H_2 at 500 °C for 1 h and cooled down to room temperature in flowing Ar. CO was introduced into the cell and then spectra were collected until the signals were stable. Ar flow was switched to purge the gaseous and weakly adsorbed CO till that the spectra were unchanged. X-ray photoelectron spectroscopy (XPS) measurements were carried out with a SPECS spectrometer equipped with an Al $\text{K}\alpha$ x-ray source operated at 300 W.

2.3. Catalytic tests

Methane oxidation reaction was evaluated in a home-built fixed bed microreactor. The products were analyzed by an on-line gas chromatograph (Agilent GC6890) equipped with a TDX-1 column and a thermal conductivity detector. 60 mg catalysts were loaded into a quartz tube, and the reaction gas consists of 0.5 % CH_4 , 2 % O_2 and He balance. Before reaction, all catalysts were pretreated in flowing pure H_2 at 500 °C for 1 h. The catalytic reaction was evaluated at 600 °C, and the conversions of CH_4 ($\text{C}(\text{CH}_4)$) and selectivity of CO_2 and CO ($\text{S}(\text{CO}_2)$, $\text{S}(\text{CO})$) were calculated as follows:

$$\text{C}(\text{CH}_4)(\%) = \left(1 - \frac{\text{moles of CH}_4 \text{ output}}{\text{moles of CH}_4 \text{ output} + \text{moles of CO}_2 \text{ output} + \text{moles of CO output}}\right) \times 100\%$$

$$S(\text{CO}_2)(\%) = \frac{\text{moles of CO}_2 \text{ output}}{\text{moles of CO}_2 \text{ output} + \text{moles of CO output}} \times 100\%$$

$$S(\text{CO})(\%) = \frac{\text{moles of CO output}}{\text{moles of CO}_2 \text{ output} + \text{moles of CO output}} \times 100\%$$

3. Results and discussion

3.1. Catalytic performance

The methane oxidation reaction data on the Ni|pBN catalyst containing a physical mixture of Ni NPs and pBN are presented in Fig. 1a. CH₄ conversion increases from 42 % to 88 % at 600 °C within 1 h, and then gradually decreases to 40 % after 20 h test. Meanwhile, the product selectivity changes from 100 % CO₂ to 80 % CO after 5 h test, and then the CO selectivity remains unchanged with the further increase of the reaction time. The reaction results show that the complete oxidation of methane to CO₂ occurs first, which is well expected on Ni-based catalysts [44,45]. In contrast, the partial oxidation of methane to CO occurs with the on-going reaction process, which has not been observed. For comparison, Ni|Al₂O₃ catalyst containing a physical mixture of Ni NPs and Al₂O₃ has been tested under the identical reaction conditions. As shown in Fig. 1b, CH₄ conversion increases from 72 % to 88 % at 600 °C within 1 h and then drops to 49 % after 20 h test. During the 20 h test only CO₂ is observed on the Ni|Al₂O₃ catalyst, which is in sharp contrast with the reaction behavior from the Ni|pBN catalyst.

3.2. Structural properties of catalysts

The changes in the product selectivity suggest the evolution of surface structure of Ni|pBN catalyst during the methane oxidation reaction. XRD patterns of the fresh and spent Ni|pBN catalysts are presented in Fig. 2a. Strong diffraction peaks for metallic Ni at 44.5° and 51.8° are observed in the fresh Ni|pBN catalyst [8]. In contrast, the spent Ni|pBN catalyst (after 20 h test at 600 °C) shows three strong diffraction peaks at 37.2°, 43.2° and 62.8° corresponding to NiO (111), (200) and (220), respectively. The disappearance of diffraction peaks of metallic Ni indicates that Ni NPs are oxidized after the methane oxidation reaction. XRD pattern of the fresh Ni|Al₂O₃ catalyst (Fig. 2b) also shows the diffraction peaks for metallic Ni at 44.5° and 51.8°, and only the diffraction peaks of NiO appear in the spent Ni|Al₂O₃ catalyst, indicating that the Ni NPs of the fresh Ni|Al₂O₃ catalyst are also oxidized after the reaction.

The fresh and spent Ni|pBN catalysts (Fig. S1a-b) are further characterized by TEM, which shows that the Ni NPs are in contact with the pBN surface, and the average size of Ni NPs is in the range of 48.7 nm (fresh) to 29.5 nm (spent). For the fresh and spent Ni|Al₂O₃ catalysts,

the average size of Ni NPs is in the range of 40.2 nm (fresh) to 30.3 nm (spent) (Fig. S2a-b). HRTEM images (Fig. 2c, S3) show that Ni NPs in the fresh Ni|pBN catalyst have bare and clean surfaces. In contrast, Ni NPs in the spent Ni|pBN catalyst are covered by amorphous overlayers (Fig. 2d, S4a-b). EDS elemental mapping analysis (Fig. 2e-h) has been further conducted and turns out that the amorphous overlayers consist of B and O elements. Thus, we conclude that the Ni NPs are encapsulated by amorphous BO_x overlayers which happens during the methane oxidation reaction. It should be noted that Ni NPs in both fresh and used Ni|Al₂O₃ catalysts present well-defined surface structures without amorphous overlayers (Figs. S5–6).

The encapsulation of metal NPs with support-derived material overlayers is a typical characteristic of the SMSI effect in oxide supported metal catalysts [12]. The classical SMSI state usually results in the suppression of surface adsorption of small molecules such as CO and H₂ [12,27], which can be well confirmed by the surface adsorption experiments. DRIFTS experiments of CO adsorption were performed over the fresh and spent Ni|pBN catalysts. As shown in Fig. 3a, two adsorption peaks on the fresh Ni|pBN catalyst centered at 2052 and 1894 cm⁻¹ are observed, both of which can be ascribed to linear and bridge CO adsorbed on metallic Ni (Ni⁰), respectively [46]. Besides, the bands at 2171 and 2116 cm⁻¹ originate from gaseous CO molecules, which disappear completely upon purging with Ar (Fig. S7). For the spent Ni|pBN catalyst, the peak intensity of linear CO adsorption on Ni⁰ at 2052 cm⁻¹ is significantly reduced, indicating that Ni NPs are encapsulated, which is consistent with the HRTEM result. On the contrary, the linear CO adsorption on Ni⁰ centered at 2057 cm⁻¹ is observed over the fresh Ni|Al=Al₂O₃ catalyst, which has no big change in the peak position and intensity after the reaction (Fig. 3b). XPS spectra in Fig. 3c demonstrate the difference in the chemical states of the fresh and spent Ni|pBN catalysts. Two kinds of boron species are corresponding to h-BN (190.3 eV) and BO_x (192.2 eV) species in both Ni|pBN catalysts [47,48]. The BO_x percentage increases from 39 % to 55 % after the reaction. Two components at 853.6 and 857.6 eV in the XPS Ni 2p_{3/2} spectrum of the fresh sample (Fig. 3d) are attributed to NiO and Ni₂O₃ species, respectively, which are due to the surface oxidation when exposed to air [49]. For the spent Ni|pBN catalyst, the shoulder peak at 863.8 eV (satellite peak) indicates the presence of more than one “nickel–oxygen” species on the catalyst surface after the reaction at 600 °C [50]. The increase in Ni 2p_{3/2} peak intensity of the spent Ni|pBN catalyst may be due to the decrease in Ni particle size after the reaction.

3.3. Evolution of the catalyst structure

The above results suggest that the methane oxidation reaction has induced a significant structural change of the Ni|pBN catalyst from bare Ni NPs to Ni NPs encapsulated with BO_x overlayers. The formation of an encapsulation structure of Ni@BO_x leads to the change in product selectivity from 100 % CO₂ to 80 % CO. This process has been illustrated in Fig. 3e. In the initial stage of the reaction, the activation of CH₄ and O₂

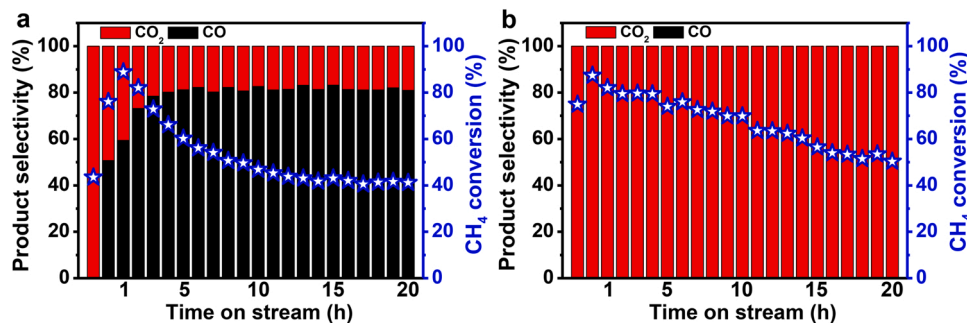


Fig. 1. CH₄ conversion and product selectivity of methane oxidation reaction over (a) Ni|pBN and (b) Ni|Al₂O₃ catalysts against time-on-stream. Reaction conditions: 1 atm, 600 °C, 0.5 % CH₄, 2 % O₂ and balanced with He; 60 mg catalyst; flow rate 10 mL·min⁻¹.

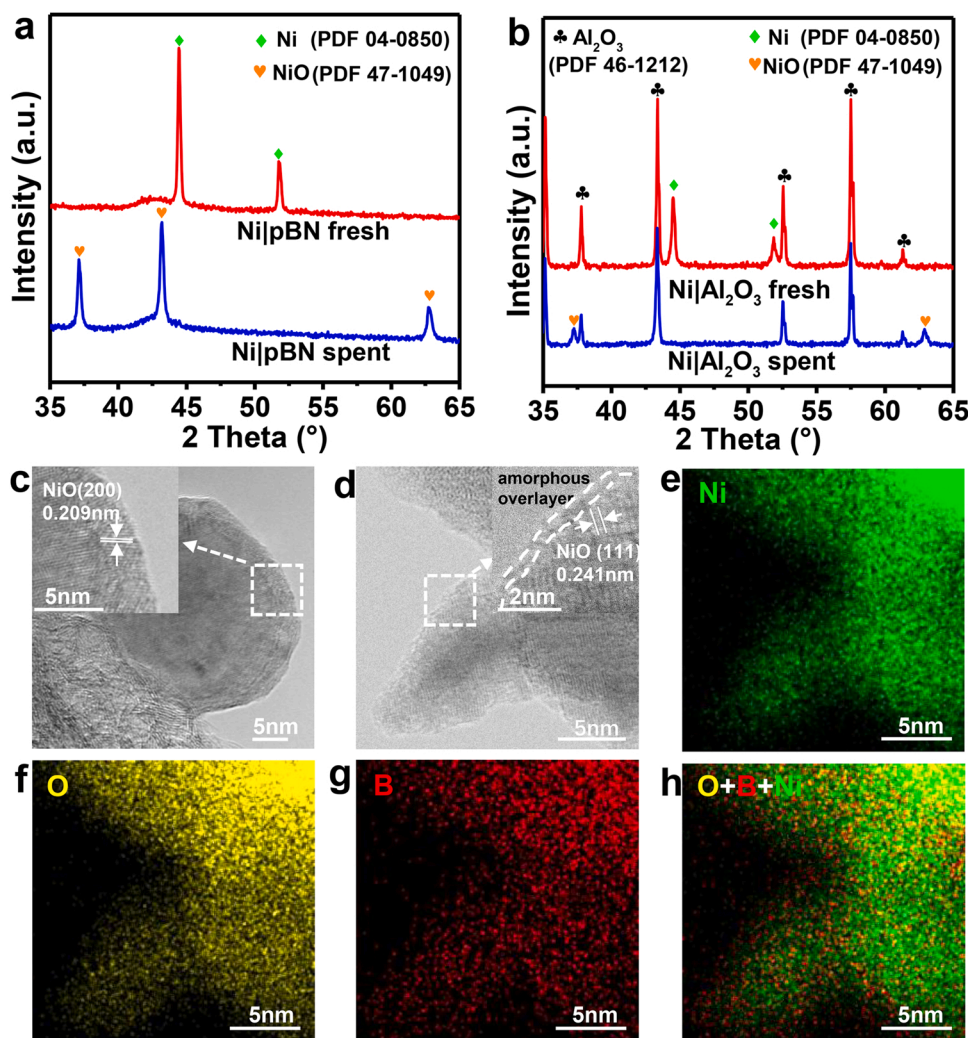


Fig. 2. (a) XRD patterns of the fresh and spent Ni|pBN catalysts. (b) XRD patterns of the fresh and spent Ni|Al₂O₃ catalysts. (c) HRTEM images of the fresh Ni|pBN catalyst. (d) HRTEM and (e-h) EDS mapping images of the spent Ni|pBN catalyst. Inset image of (c) and (d) show NiO (200) and NiO (111) lattice spacing, respectively. For the electron microscopy analysis, each sample was pretreated with air at 300 °C for 2 h in order to exclude the influence of surface contaminating carbon overlayers.

occurs on the surface of bare Ni NPs. CO₂ and H₂O are generated via combustion of methane. At the same time, more BO_x species (Fig. 3c) are formed with the methane oxidation reaction. The produced BO_x species may gradually migrate onto Ni NPs to form BO_x encapsulation overlayers. Consequently, the reaction will mainly take place on the surface of BO_x overlayers, in which molecular O₂ bonded to surface coordinatively unsaturated BO₃ centers acts as a judicious oxidant for methane activation with mitigated CO₂ formation [51].

In order to observe the formation of the SMSI state between Ni NPs and pBN more clearly, it is necessary to slow down the formation process. Therefore, reducing the contact area between Ni NPs and pBN has been further attempted. Here, pBN was added as a diluent to a Ni/Al₂O₃ catalyst, which were mixed by shaking them in a reaction tube (denoted as Ni/Al₂O₃|pBN, Fig. 4a). SEM and EDS mapping images (Fig. S8) show that Ni NPs of Ni/Al₂O₃ and pBN are distributed in the Ni/Al₂O₃|pBN catalyst without direct contact. This catalyst is treated under the same reaction conditions as applied before for the Ni|pBN catalyst. Interestingly, changes in product selectivity from CO₂ to CO can still be observed during the reaction over the Ni/Al₂O₃|pBN catalyst (Fig. 4b). Within 6 h of the reaction at 600 °C the product is 100 % CO₂. After 6 h the selectivity of CO gradually increases and finally gets stabilized at 75 %, while CH₄ conversion decreases from 100 % to 59 % after 42 h test. For comparison, Ni/Al₂O₃, pure Al₂O₃ and pBN catalysts have also been tested under the same reaction conditions. For the Ni/Al₂O₃ catalyst (Fig. 4c), only CO₂ is observed and CH₄ conversion decreases from 100 % to 72 % after 42 h test. Pure Al₂O₃ has quite low methane oxidation

activity (Fig. S9). CH₄ conversion decreases from 93 % to 3 % over the pure pBN catalyst with 72 % CO selectivity after 42 h test (Fig. 4d), suggesting that strong deactivation happens in the pBN-catalyzed process. These results confirm that the addition of pBN plays a key role in the modulation of product selectivity from CO₂ to CO during Ni-catalyzed methane oxidation at 600 °C.

SEM and Elemental mapping images (Fig. 5a-e, S10) of the spent Ni/Al₂O₃|pBN catalyst display that Ni NPs are still located on Al₂O₃ without direct contact with pBN. HRTEM images of the fresh Ni/Al₂O₃|pBN catalyst show clean Ni particle surface (Fig. S11). After the reaction, the surface of Ni NPs supported on Al₂O₃ is covered by an amorphous overlayer (Fig. 5f, S12). Elemental mapping analysis (Fig. 5g-j, S13) of the spent Ni/Al₂O₃|pBN catalyst confirms that the overlayer has B and O components, indicating the migration of BO_x species from pBN to the surface of Ni NPs on Al₂O₃ to form an encapsulation overlayer. It should be noted that B signals can be observed in the alumina supports, indicating that the support surfaces may be also covered by B-containing species.

DRIFTS spectra of CO adsorption (Fig. 6a) show that CO adsorption bands at 2047 and 1910 cm⁻¹ attributed to linear and bridge CO adsorbed on Ni⁰ have been detected over the fresh Ni/Al₂O₃|pBN catalyst but no these CO adsorption bands on the spent Ni/Al₂O₃|pBN catalyst. XPS B 1 s spectra of the fresh and spent Ni/Al₂O₃|pBN catalysts are shown in Fig. 6b, indicating that the proportion of surface BO_x species gradually increases with the increasing reaction time. The surface chemistry studies further confirm that the methane oxidation

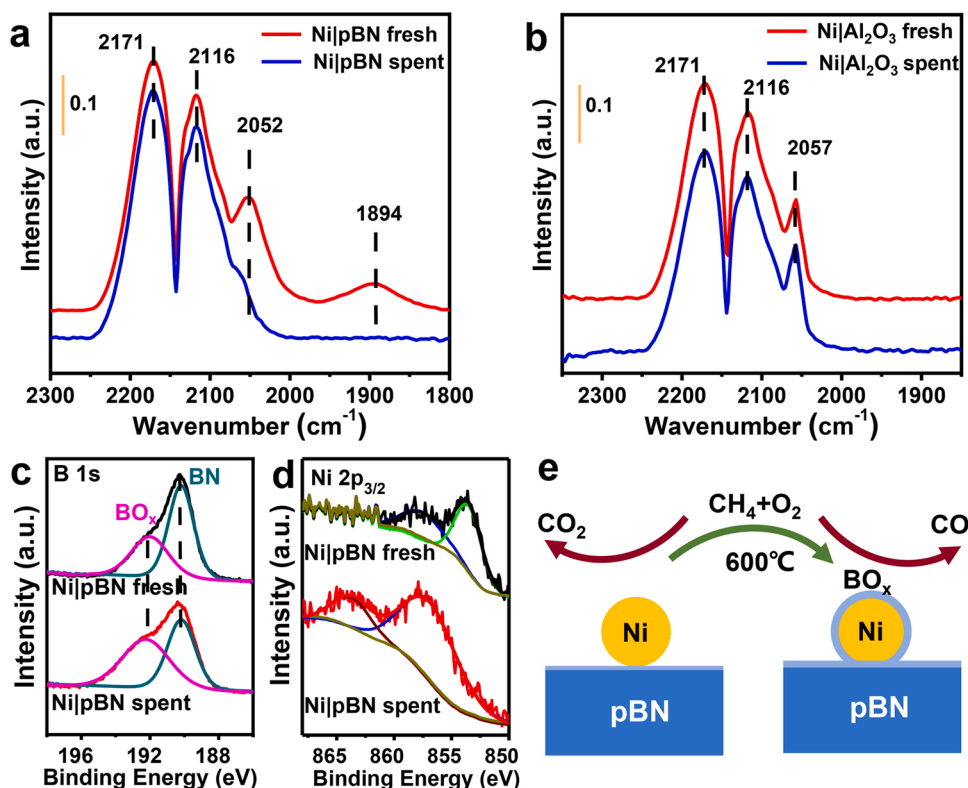


Fig. 3. (a) DRIFTS spectra of CO adsorption on fresh and spent Ni|pBN catalysts. (b) DRIFTS spectra of CO adsorption on fresh and spent Ni|Al₂O₃ catalysts. Before collecting CO adsorption signals, each sample was pretreated in pure H₂ at 500 °C for 1 h. (c) B 1s and (d) Ni 2p_{3/2} spectra of fresh and spent Ni|pBN catalysts. (e) Schematic diagram of the structural change of Ni|pBN catalyst from the bare Ni NPs to encapsulated Ni NPs with BO_x overlayers (Ni@BO_x|pBN) during methane oxidation reaction.

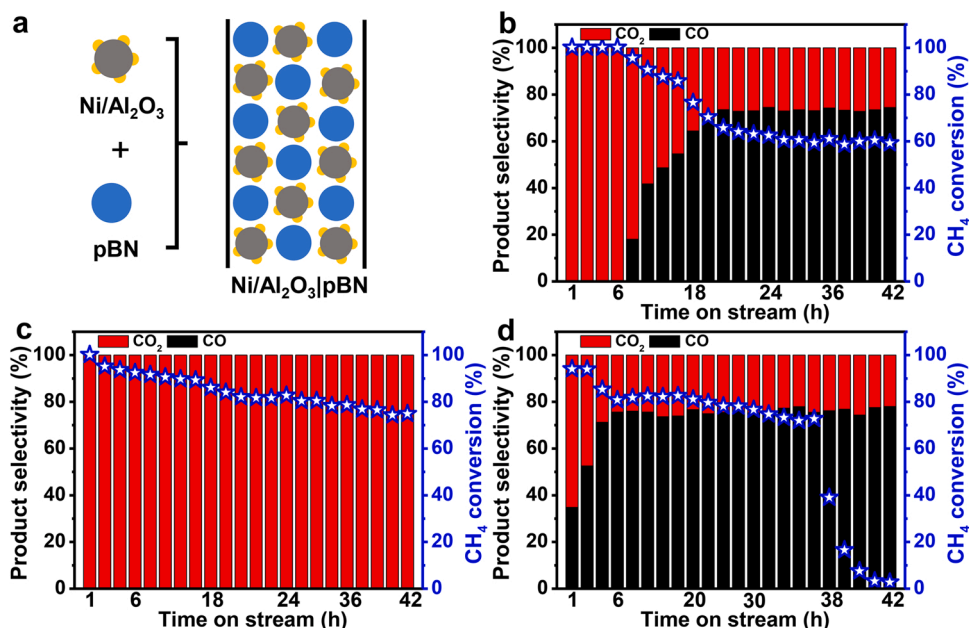


Fig. 4. (a) Schematic diagram of Ni/Al₂O₃|pBN catalyst. CH₄ conversion and product selectivity of methane oxidation reaction over (b) Ni/Al₂O₃|pBN, (c) Ni/Al₂O₃ and (d) pBN catalysts against time-on-stream. Reaction conditions: 1 atm; 600 °C, 0.5 % CH₄, 2 % O₂ and balanced with He; (b) 60 mg Ni/Al₂O₃|30 mg pBN, (c) 60 mg Ni/Al₂O₃ and (d) 30 mg pBN; flow rate 10 mL·min⁻¹.

atmosphere indeed induces encapsulation of Ni NPs by BO_x species in the Ni/Al₂O₃|pBN catalyst.

3.4. Proposed formation mechanism for SMSI state (Ni@BO_x)

We have observed the SMSI state (Ni@BO_x) in the Ni/Al₂O₃|pBN catalyst during the methane oxidation at 600 °C, which alters the

product selectivity of Ni-catalyzed methane oxidation. Ni NPs and pBN are distributed in the Ni/Al₂O₃|pBN catalyst without direct contact and, therefore, the occurrence of the SMSI state strongly suggests the vapor migration of boron-containing species from pBN component to surfaces of Ni NPs. It is known that both BN and BO_x species are very difficult to evaporate for direct gas phase migration [52]. Considering that the boron oxides can form volatile boric acid in the presence of high

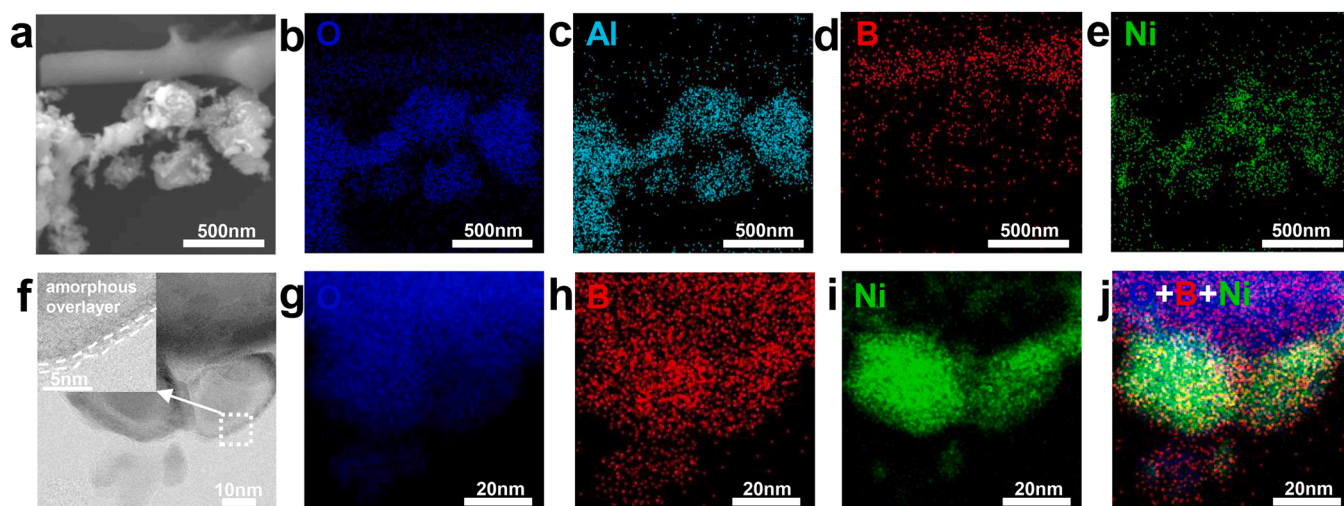


Fig. 5. (a) SEM image of spent Ni/Al₂O₃|pBN catalyst and (b-e) Elemental mapping images of the region shown in (a). (f) HRTEM image of spent Ni/Al₂O₃|pBN catalyst. Inset image shows is a close-up of the marked area in (f). (g-i) Elemental mapping images of the region shown in (f). Before electron microscopy analysis, each sample was pretreated with air at 300 °C for 2 h in order to exclude the influence of contaminating carbon overlayers.

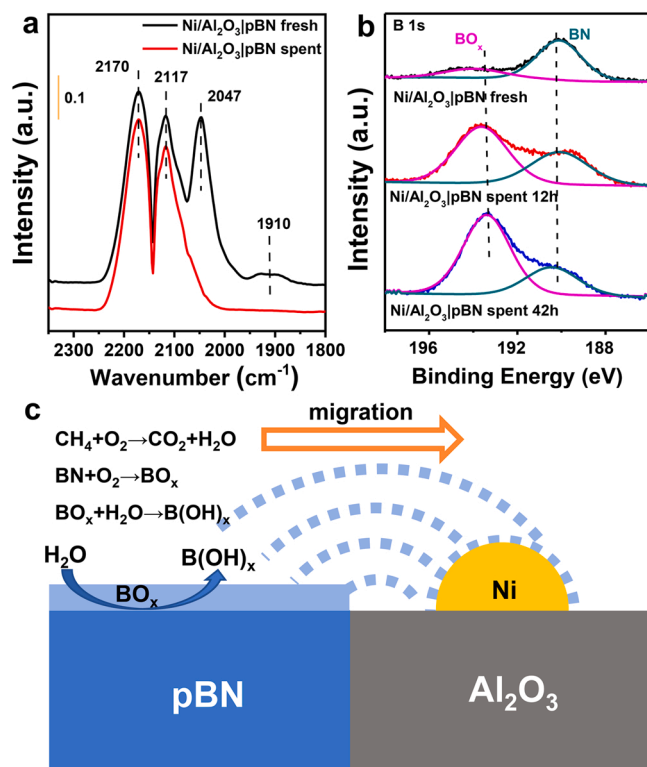


Fig. 6. (a) DRIFTS spectra of CO adsorption and (b) XPS B 1s spectra of Ni/Al₂O₃|pBN catalyst before and after methane oxidation reaction. Before collecting CO adsorption signals, each sample was pretreated in pure H₂ at 500 °C for 1 h. (c) Schematic illustration of the migration of BO_x species from pBN to the surface of Ni NPs of Ni/Al₂O₃|pBN during methane oxidation reaction.

temperature water vapor [53], we suggest that the SMSI between Ni NPs and pBN may be achieved by high temperature-induced vapor migration of B(OH)_x species.

To prove this hypothesis, some confirmatory experiments have been carried out. The dehydrated commercial boron oxide powder was treated in 3 % H₂O/Ar at 600 °C for 12 h, and its mass was reduced by 9.2 % after the treatment. At the same time, boric acid was found to deposit onto the inner wall of the quartz tube at the exhaust end

(Fig. S14), which proves that boron oxide can react with water vapor to generate volatile boric acid. As a comparison, pBN powder was first treated in O₂ at 600 °C for 12 h and its mass was increased by 5.4 % due to the oxidation of pBN into BO_x. Then, the oxidized pBN powder was further treated in H₂O/Ar at 600 °C for 20 h and its mass was decreased by 12.2 %. Meanwhile, boric acid was also formed on the inner tube wall at the end of the quartz tube after the treatment (Fig. S15). The control experiments indicate that BO_x species on the pBN surface can form volatile B(OH)_x species in the presence of high temperature water vapor.

According to the above results, the formation of the SMSI state can be illustrated in Fig. 6c. In the initial stage of the reaction, the combustion reaction of methane preferentially occurs on Ni/Al₂O₃ to generate CO₂ and water vapor. At the same time, the pBN surface is partially oxidized to generate a large amount of BO_x species, which further react with the generated water vapor to produce volatile B(OH)_x. As the reaction time increases, the volatile B(OH)_x can gradually migrate onto the surface of Ni NPs supported on Al₂O₃ to form encapsulation overlayers, which continues to act as active sites to activate CH₄ and O₂ [51]. Interestingly, the BO_x overlayers migrated onto the Ni NPs of Ni/Al₂O₃|pBN catalyst have better activity and stability than the BO_x species on the pBN (Fig. S16) during the reaction at 600 °C (Figs. 4b, d and S17), which may indicate that Ni NPs also play a certain role in the reaction in addition to the function as a support to disperse and stabilize the BO_x species. Here, given the lower melting point of boron oxide (around 450 °C), defects and pores may exist in the BO_x overlayers, which allow the reactants to access the surface of Ni NPs. Therefore, Ni helps dissociate CH₄ to generate CH_x and H, and H adsorbs onto BO_x species to form B-O-H active sites. Then, CH_x reacts with B-O-H to generate CH_xOH, which is further decomposed to CO and H₂. So, Ni NPs may work synergistically with the BO_x/B(OH)_x species in the methane oxidation reaction [11,51, 54].

4. Conclusions

We have observed the occurrence of the classical SMSI state in both Ni|pBN and Ni/Al₂O₃|pBN catalysts in methane oxidation at 600 °C, in which Ni NPs are only physically mixed with pBN. The BO_x species from pBN can migrate onto Ni NPs to form the encapsulation structure (Ni@BO_x) during the reaction, resulting in the switch of the reaction selectivity from CO₂ (on the exposed Ni NPs) to CO (on the Ni@BO_x NPs). Since Ni NPs are not in close contact with pBN or even with no direct contact with pBN in these catalysts, the formation of the BO_x encapsulation overlayers indicates the vapor migration of boron-

containing species from pBN to metal surfaces, in which both high reaction temperature and water product play an important role. Our study reveals a novel mechanism for the formation of encapsulation overlayers on metal nanoparticles under the SMSI state.

CRedit authorship contribution statement

Tongyuan Song: Investigation, Visualization, Writing – original draft. **Rongtan Li:** Investigation. **Jianyang Wang:** Investigation. **Cui Dong:** Investigation. **Xiaohui Feng:** Investigation. **Shiwen Li:** Investigation. **Qiang Fu:** Conceptualization, Methodology, Writing – review & editing, Supervision.

Declaration of Competing Interest

The authors declare that they have no known competing financial interests or personal relationships that could have appeared to influence the work reported in this paper.

Data Availability

Data will be made available on request.

Acknowledgements

This work was financially supported by the National Key R&D Program of China (2021YFA1502800), the National Natural Science Foundation of China (nos. 21825203, 22288201, and 91945302), the Photon Science Center for Carbon Neutrality, LiaoNing Revitalization Talents Program (XLYC1902117), and the Dalian National Laboratory for Clean Energy (DNL) Cooperation Fund (DNL201907).

Conflicts of interest

The authors declare no competing financial interest.

Appendix A. Supporting information

Supplementary data associated with this article can be found in the online version at [doi:10.1016/j.apcatb.2022.122021](https://doi.org/10.1016/j.apcatb.2022.122021).

References

- [1] T.V. Choudhary, V.R. Choudhary, Energy-efficient syngas production through catalytic oxy-methane reforming reactions, *Angew. Chem. Int. Ed.* 47 (2008) 1828–1847.
- [2] R.J. Farrauto, Low-temperature oxidation of methane, *Science* 337 (2012) 659–660.
- [3] P. Gelin, M. Primet, Complete oxidation of methane at low temperature over noble metal based catalysts: a review, *Appl. Catal. B-Environ.* 39 (2002) 1–37.
- [4] B.C. Enger, R. Lodeng, A. Holmen, A review of catalytic partial oxidation of methane to synthesis gas with emphasis on reaction mechanisms over transition metal catalysts, *Appl. Catal. A-Gen.* 346 (2008) 1–27.
- [5] Y. Kim, S. Kang, D. Kang, K.R. Lee, C.K. Song, J. Sung, J.S. Kim, H. Lee, J. Park, J. Yi, Single-phase formation of Rh₂O₃ nanoparticles on h-BN support for highly controlled methane partial oxidation to syngas, *Angew. Chem. -Int. Ed.* 60 (2021) 25411–25418.
- [6] R.K. Singha, A. Shukla, A. Yadav, L.S. Konathala, R. Bal, Effect of metal-support interaction on activity and stability of Ni-CeO₂ catalyst for partial oxidation of methane, *Appl. Catal. B-Environ.* 202 (2017) 473–488.
- [7] A. Löfberg, J. Guerrero-Caballero, T. Kane, A. Rubbens, L. Jalowiecki-Duhamel, Ni/CeO₂ based catalysts as oxygen vectors for the chemical looping dry reforming of methane for syngas production, *Appl. Catal. B-Environ.* 212 (2017) 159–174.
- [8] Y. Cao, P. Maitarad, M. Gao, T. Taketsugu, H. Li, T. Yan, L. Shi, D. Zhang, Defect-induced efficient dry reforming of methane over two-dimensional Ni/h-boron nitride nanosheet catalysts, *Appl. Catal. B-Environ.* 238 (2018) 51–60.
- [9] M.M. Pakulska, C.M. Grgicak, J.B. Giorgi, The effect of metal and support particle size on NiO/CeO₂ and NiO/ZrO₂ catalyst activity in complete methane oxidation, *Appl. Catal. A-Gen.* 332 (2007) 124–129.
- [10] R.K. Singha, A. Yadav, A. Agrawal, A. Shukla, S. Adak, T. Sasaki, R. Bal, Synthesis of highly coke resistant Ni nanoparticles supported MgO/ZnO catalyst for reforming of methane with carbon dioxide, *Appl. Catal. B-Environ.* 191 (2016) 165–178.
- [11] J. Dong, Q. Fu, H. Li, J. Xiao, B. Yang, B. Zhang, Y. Bai, T. Song, R. Zhang, L. Gao, Reaction-induced strong metal-support interactions between metals and inert boron nitride nanosheets, *J. Am. Chem. Soc.* 142 (2020) 17167–17174.
- [12] S. Tauster, S. Fung, R.L. Garten, Strong metal-support interactions. Group 8 noble metals supported on titanium dioxide, *J. Am. Chem. Soc.* 100 (1978) 170–175.
- [13] J. Liu, Advanced electron microscopy of metal-support interactions in supported metal catalysts, *ChemCatChem* 3 (2011) 934–948.
- [14] T.W. van Deelen, C. Hernández Mejía, K.P. de Jong, Control of metal-support interactions in heterogeneous catalysts to enhance activity and selectivity, *Nat. Catal.* 2 (2019) 955–970.
- [15] Y. Li, Y. Zhang, K. Qian, W. Huang, Metal-support interactions in metal/oxide catalysts and oxide-metal interactions in oxide/metal inverse catalysts, *ACS Catal.* 12 (2022) 1268–1287.
- [16] H. Frey, A. Beck, X. Huang, J.A. van Bokhoven, M.-G. Willinger, Dynamic interplay between metal nanoparticles and oxide support under redox conditions, *Science* 376 (2022) 982–987.
- [17] S. Bernal, J. Calvino, M. Cauqui, J. Gatica, C.L. Cartes, J.P. Omil, J. Pintado, Some contributions of electron microscopy to the characterisation of the strong metal-support interaction effect, *Catal. Today* 77 (2003) 385–406.
- [18] Q. Fu, T. Wagner, S. Olliges, H.-D. Carstanjen, Metal-oxide interfacial reactions: encapsulation of Pd on TiO₂ (110), *J. Phys. Chem. B* 109 (2005) 944–951.
- [19] Y. Kuwauchi, H. Yoshida, T. Akita, M. Haruta, S. Takeda, Intrinsic catalytic structure of gold nanoparticles supported on TiO₂, *Angew. Chem. -Int. Ed.* 51 (2012) 7729–7733.
- [20] M.G. Willinger, W. Zhang, O. Bondarchuk, S. Shaikhutdinov, H.J. Freund, R. Schlögl, A case of strong metal-support interactions: combining advanced microscopy and model systems to elucidate the atomic structure of interfaces, *Angew. Chem. -Int. Ed.* 53 (2014) 5998–6001.
- [21] S. Zhang, P.N. Plessow, J.J. Willis, S. Dai, M. Xu, G.W. Graham, M. Cargnello, F. Abild-Pedersen, X. Pan, Dynamical observation and detailed description of catalysts under strong metal-support interaction, *Nano Lett.* 16 (2016) 4528–4534.
- [22] X. Xu, Q. Fu, L. Gan, J. Zhu, X. Bao, Interface-confined FeO_x adlayers induced by metal support interaction in Pt/FeO_x catalysts, *J. Phys. Chem. B* 122 (2018) 984–990.
- [23] A. Beck, X. Huang, L. Artiglia, M. Zabilskiy, X. Wang, P. Rzepka, D. Palagin, M.-G. Willinger, J.A. van Bokhoven, The dynamics of overlayer formation on catalyst nanoparticles and strong metal-support interaction, *Nat. Commun.* 11 (2020) 3220–3227.
- [24] G.L. Haller, D.E. Resasco, Metal-support interaction: group VIII metals and reducible oxides, *Advances in Catalysis*, Elsevier, 1989, pp. 173–235.
- [25] C. Hernández Mejía, T.W. van Deelen, K.P. de Jong, Activity enhancement of cobalt catalysts by tuning metal-support interactions, *Nat. Commun.* 9 (2018) 4459–4466.
- [26] M. Xu, S. Yao, D. Rao, Y. Niu, N. Liu, L. Zheng, B. Wang, B. Zhang, D. Ma, M. Wei, Insights into interfacial synergistic catalysis over Ni@TiO_{2-x} catalyst toward water-gas shift reaction, *J. Am. Chem. Soc.* 140 (2018) 11241–11251.
- [27] S. Tauster, Strong metal-support interactions, *Acc. Chem. Res.* 20 (1987) 389–394.
- [28] H. Tang, Y. Su, B. Zhang, A.F. Lee, M.A. Isaacs, K. Wilson, L. Li, Y. Ren, J. Huang, M. Haruta, Classical strong metal-support interactions between gold nanoparticles and titanium dioxide, *Sci. Adv.* 3 (2017), e1700231.
- [29] A. Corma, P. Serna, P. Concepción, J.J. Calvino, Transforming nonselective into chemoselective metal catalysts for the hydrogenation of substituted nitroaromatics, *J. Am. Chem. Soc.* 130 (2008) 8748–8753.
- [30] J.C. Matsubu, S. Zhang, L. DeRita, N.S. Marinkovic, J.G. Chen, G.W. Graham, X. Pan, P. Christopher, Adsorbate-mediated strong metal-support interactions in oxide-supported Rh catalysts, *Nat. Chem.* 9 (2017) 120–127.
- [31] H. Tang, F. Liu, J. Wei, B. Qiao, K. Zhao, Y. Su, C. Jin, L. Li, J. Liu, J. Wang, Ultrastable hydroxyapatite/titanium-dioxide-supported gold nanocatalyst with strong metal-support interaction for carbon monoxide oxidation, *Angew. Chem. -Int. Ed.* 128 (2016) 10764–10769.
- [32] Y. Zhang, J.X. Liu, K. Qian, A. Jia, D. Li, L. Shi, J. Hu, J. Zhu, W. Huang, Structure sensitivity of Au-TiO₂ strong metal-support interactions, *Angew. Chem. -Int. Ed.* 60 (2021) 12074–12081.
- [33] H. Xin, L. Lin, R. Li, D. Li, T. Song, R. Mu, Q. Fu, X. Bao, Overturning CO₂ hydrogenation selectivity with high activity via reaction-induced strong metal-support interactions, *J. Am. Chem. Soc.* 144 (2022) 4874–4882.
- [34] X. Liu, M.-H. Liu, Y.-C. Luo, C.-Y. Mou, S.D. Lin, H. Cheng, J.-M. Chen, J.-F. Lee, T.-S. Lin, Strong metal-support interactions between gold nanoparticles and ZnO nanorods in CO oxidation, *J. Am. Chem. Soc.* 134 (2012) 10251–10258.
- [35] S. Liu, W. Xu, Y. Niu, B. Zhang, L. Zheng, W. Liu, L. Li, J. Wang, Ultrastable Au nanoparticles on titania through an encapsulation strategy under oxidative atmosphere, *Nat. Commun.* 10 (2019) 5790–5798.
- [36] T. Song, J. Dong, R. Li, X. Xu, M. Hiroaki, B. Yang, R. Zhang, Y. Bai, H. Xin, L. Lin, Oxidative strong metal-support interactions between metals and inert boron nitride, *J. Phys. Chem. Lett.* 12 (2021) 4187–4194.
- [37] H. Wang, L. Wang, D. Lin, X. Feng, Y. Niu, B. Zhang, F.-S. Xiao, Strong metal-support interactions on gold nanoparticle catalysts achieved through Le Chatelier's principle, *Nat. Catal.* 4 (2021) 418–424.
- [38] H. Chen, Z. Yang, X. Wang, F. Polo-Garzon, P.W. Halstenberg, T. Wang, X. Suo, S.-Z. Yang, H.M. Meyer III, Z. Wu, Photoinduced strong metal-support interaction for enhanced catalysis, *J. Am. Chem. Soc.* 143 (2021) 8521–8526.
- [39] J. Sheng, W.-C. Li, W.-D. Lu, B. Yan, B. Qiu, X.-Q. Gao, R.-P. Zhang, S.-Z. Zhou, A.-H. Lu, Preparation of oxygen reactivity-tuned FeO_x/BN catalyst for selectively oxidative dehydrogenation of ethylbenzene to styrene, *Appl. Catal. B-Environ.* 305 (2022), 121070.

- [40] T. Fujitani, T. Matsuda, Y. Kushida, S. Ogiwara, T. Uchijima, J. Nakamura, Creation of the active site for methanol synthesis on a Cu/SiO₂ catalyst, *Catal. Lett.* 49 (1997) 175–179.
- [41] X. Zhang, P. Yan, B. Zhao, K. Liu, M.C. Kung, H.H. Kung, S. Chen, Z.C. Zhang, Selective hydrodeoxygenation of guaiacol to phenolics by Ni/anatase TiO₂ catalyst formed by cross-surface migration of Ni and TiO₂, *ACS Catal.* 9 (2019) 3551–3563.
- [42] Q. Weng, X. Wang, C. Zhi, Y. Bando, D. Golberg, Boron nitride porous microbelts for hydrogen storage, *ACS Nano* 7 (2013) 1558–1565.
- [43] S. Chen, P. Li, S. Xu, X. Pan, Q. Fu, X. Bao, Carbon doping of hexagonal boron nitride porous materials toward CO₂ capture, *J. Mater. Chem. A* 6 (2018) 1832–1839.
- [44] F. Liu, Y. Sang, H. Ma, Z. Li, Z. Gao, Nickel oxide as an effective catalyst for catalytic combustion of methane, *J. Nat. Gas. Sci. Eng.* 41 (2017) 1–6.
- [45] J. Chen, T. Buchanan, E.A. Walker, T.J. Toops, Z. Li, P. Kunal, E.A. Kyriakidou, Mechanistic understanding of methane combustion over Ni/CeO₂: a combined experimental and theoretical approach, *ACS Catal.* 11 (2021) 9345–9354.
- [46] C. Hu, Y. Chen, P. Li, H. Min, Y. Chen, A. Tian, Temperature-programmed FT-IR study of the adsorption of CO and co-adsorption of CO and H₂ on Ni/Al₂O₃, *J. Mol. Catal. A-Chem.* 110 (1996) 163–169.
- [47] A.S. Konopatsky, K.L. Firestein, D.V. Leybo, Z.I. Popov, K.V. Larionov, A. E. Steinman, A.M. Kovalskii, A.T. Matveev, A.M. Manakhov, P.B. Sorokin, BN nanoparticle/Ag hybrids with enhanced catalytic activity: theory and experiments, *Catal. Sci. Technol.* 8 (2018) 1652–1662.
- [48] A.M. Kovalskii, I.N. Volkov, N.D. Evdokimenko, O.P. Tkachenko, D.V. Leybo, I. V. Chepkasov, Z.I. Popov, A.T. Matveev, A. Manakhov, E.S. Permyakova, D. V. Golberg, D.V. Shtansky, Hexagonal BN-and BNO-supported Au and Pt nanocatalysts in carbon monoxide oxidation and carbon dioxide hydrogenation reactions, *Appl. Catal. B-Environ.* 303 (2022), 120891.
- [49] J. Schreieffels, P. Maybury, W. Swartz Jr, X-ray photoelectron spectroscopy of nickel boride catalysts: correlation of surface states with reaction products in the hydrogenation of acrylonitrile, *J. Catal.* 65 (1980) 195–206.
- [50] M. Lewandowski, Hydrotreating activity of bulk NiB alloy in model reaction of hydrodenitrogenation of carbazole, *Appl. Catal. B-Environ.* 168 (2015) 322–332.
- [51] J. Tian, J. Tan, Z. Zhang, P. Han, M. Yin, S. Wan, J. Lin, S. Wang, Y. Wang, Direct conversion of methane to formaldehyde and CO on B₂O₃ catalysts, *Nat. Commun.* 11 (2020) 5693–5699.
- [52] A.T. Matveev, K.L. Firestein, A.E. Steinman, A.M. Kovalskii, O.I. Lebedev, D. V. Shtansky, D. Golberg, Boron nitride nanotube growth via boron oxide assisted chemical vapor transport-deposition process using LiNO₃ as a promoter, *Nano Res.* 8 (2015) 2063–2072.
- [53] M. Steinbrück, Oxidation of boron carbide at high temperatures, *J. Nucl. Mater.* 336 (2005) 185–193.
- [54] Y. Wang, L. Zhao, L. Shi, J. Sheng, W. Zhang, X.-M. Cao, P. Hu, A.-H. Lu, Methane activation over a boron nitride catalyst driven by in situ formed molecular water, *Catal. Sci. Technol.* 8 (2018) 2051–2055.